Calcium isotope constraints on the end-Permian mass extinction

Jonathan L. Payne[a,1], Alexandra V. Turchyn[b], Adina Paytan[c], Donald J. DePaolo[d], Daniel J. Lehrmann[e], Meiyi Yu[f], and Jiayong Wei[g]

[a]Department of Geological and Environmental Sciences, Stanford University, 450 Serra Mall, Building 320, Stanford, CA 94305; [b]Department of Earth Sciences, Cambridge University, Downing Street, Cambridge, CB2 3EQ, United Kingdom; [c]Institute of Marine Sciences, University of California, Santa Cruz, CA 95064; [d]Department of Earth and Planetary Science, University of California, 301 McCone Hall, Berkeley, CA 94720-4767; [e]Department of Geology, University of Wisconsin, 800 Algoma Boulevard, Oshkosh, WI 54901; [f]College of Resource and Environment Engineering, Guizhou University, Caijiaguan, Guiyang 550003, Guizhou Province, China; and [g]Guizhou Geological Survey, Bagongli, Guiyang 550005, Guizhou Province, China

Edited by Andrew H. Knoll, Harvard University, Cambridge, MA, and approved April 1, 2010 (received for review December 4, 2009)

The end-Permian mass extinction horizon is marked by an abrupt shift in style of carbonate sedimentation and a negative excursion in the carbon isotope ($\delta^{13}C$) composition of carbonate minerals. Several extinction scenarios consistent with these observations have been put forward. Secular variation in the calcium isotope ($\delta^{44/40}Ca$) composition of marine sediments provides a tool for distinguishing among these possibilities and thereby constraining the causes of mass extinction. Here we report $\delta^{44/40}Ca$ across the Permian-Triassic boundary from marine limestone in south China. The $\delta^{44/40}Ca$ exhibits a transient negative excursion of ~0.3‰ over a few hundred thousand years or less, which we interpret to reflect a change in the global $\delta^{44/40}Ca$ composition of seawater. CO_2-driven ocean acidification best explains the coincidence of the $\delta^{44/40}Ca$ excursion with negative excursions in the $\delta^{13}C$ of carbonates and organic matter and the preferential extinction of heavily calcified marine animals. Calcium isotope constraints on carbon cycle calculations suggest that the average $\delta^{13}C$ of CO_2 released was heavier than −28‰ and more likely near −15‰; these values indicate a source containing substantial amounts of mantle- or carbonate-derived carbon. Collectively, the results point toward Siberian Trap volcanism as the trigger of mass extinction.

An abrupt shift in style of carbonate sedimentation occurs across the end-Permian extinction horizon. Microbialites and oolites overlie diverse, fossiliferous limestones of the latest Permian age in carbonate strata deposited across the tropical Tethys (1–8) and in the Panthalassa Ocean (8, 9) (Fig. S1). The mass extinction and facies shift are associated with a large negative excursion in the carbon isotope ($\delta^{13}C$) composition of carbonate minerals.

Geochemical and sedimentary observations have been used to support various causal mechanisms for the mass extinction. Three different scenarios have been put forth. First, the "Strangelove Ocean" scenario links mass extinction to collapse of the biological pump—the vertical separation in the water column of carbon fixation and respiration, which results from the sinking of organic matter out of the surface ocean (10). Under this scenario, an initial decrease in carbonate deposition would occur because of mixing of surface waters with $CaCO_3$-undersaturated deeper waters (assuming an oxygenated deep ocean); subsequent increase in alkalinity because of continental weathering would lead to enhanced carbonate deposition, explaining the deposition of microbialites and oolites (10). Second, the ocean overturn model proposes that extensive sulfate reduction in anoxic deep waters of the Permian oceans resulted in a buildup of carbonate alkalinity and hydrogen sulfide in deep water prior to the extinction event (11–14). Upwelling of these alkaline deep waters would have triggered carbonate precipitation on the shelves (2, 5, 15, 16) and caused mass extinction through combined stresses of hypercapnia, anoxia, and hydrogen sulfide poisoning (14, 15, 17). Third, the ocean acidification model proposes that massive release of ^{13}C-depleted carbon from a reservoir in the crust (e.g., methane clathrates, coal, and magma) (18–22) acidified the ocean, reducing carbonate sedimentation and potentially leading to dissolution of carbonate sediments (8). Subsequently enhanced continental weathering and consequent delivery of carbonate alkalinity to the oceans would account for the widespread deposition of microbialites and oolites above the extinction horizon (8).

One avenue for distinguishing among these hypotheses lies in their differing implications for the global cycling of calcium, an element with a residence time of approximately 600–1,000 ky and uniform isotope composition in the modern oceans (23, 24). Isotopes of calcium are fractionated during the precipitation of calcium carbonate (25–27): ^{40}Ca is preferentially incorporated into the solid phase, leaving seawater enriched in ^{44}Ca at steady state relative to the delivery and burial fluxes (24, 28). Consequently, scenarios that require imbalances between the delivery and burial fluxes of calcium in the oceans should impart changes in the calcium isotope composition in the oceans and associated sediments.

We constructed a one-box, isotope mass-balance model of the global calcium cycle (see *Methods* and *SI Discussion*) to generate quantitative predictions for marine calcium isotopes and concentrations associated with the various Permian-Triassic (P/T) boundary scenarios. Fig. 1 illustrates the predictions for these scenarios as well as two alternative possibilities requiring a shift in calcium isotopes only. Both the Strangelove Ocean and acidification scenarios predict an initial decrease in the carbonate depositional flux followed by an increase in carbonate deposition to return the system to steady state, but the perturbation is potentially much larger under the acidification scenario. In contrast, under the ocean overturn scenario one would expect a positive excursion in $\delta^{44/40}Ca$ because of the stimulation of carbonate precipitation by upwelling of alkaline deep water (2, 5, 15). Oceanographic mechanisms allowing for the overturn scenario have been debated (29–31); here we consider its implications for calcium isotopes irrespective of its feasibility from an oceanographic standpoint. A permanent global shift from calcite- to aragonite-dominated carbonate deposition across the extinction horizon is capable of producing $\delta^{44/40}Ca$ variation similar to that predicted under the acidification scenario; it causes no change in the calcium concentration of the ocean. A global shift in the isotope composition of the calcium delivery flux within the range of likely values would cause a much smaller and more gradual change in

Author contributions: J.L.P., A.V.T., and A.P. designed research; J.L.P., A.V.T., D.J.D., D.J.L., M.Y., and J.W. performed research; J.L.P., A.V.T., A.P., and D.J.D. analyzed data; and J.L.P., A.V.T., A.P., D.J.D., and D.J.L. wrote the paper.

The authors declare no conflict of interest.

This article is a PNAS Direct Submission.

Freely available online through the PNAS open access option.

[1]To whom correspondence should be addressed. E-mail: jlpayne@stanford.edu.

This article contains supporting information online at www.pnas.org/lookup/suppl/doi:10.1073/pnas.0914065107/-/DCSupplemental.

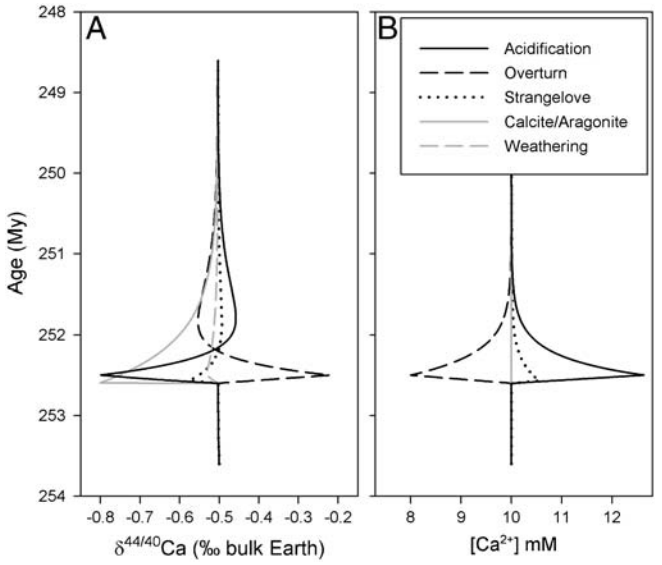

Fig. 1. Output from calcium cycle model under scenarios proposed to explain the P/T boundary $\delta^{13}C$ excursion and associated deposition of carbonate microbialites and oolites. (*A*) $\delta^{44/40}Ca$ in carbonate rocks. (*B*) Calcium concentration in seawater. The overturn and acidification scenarios are shown under an assumption of a 100-ky perturbation. Also shown are $\delta^{44/40}Ca$ predictions for a permanent increase by 50% in the proportion of aragonite in carbonate sediment and a 100-ky decrease in the $\delta^{44/40}Ca$ of the river calcium flux by 0.3‰. Modeled calcium concentrations do not change under these last two scenarios. Additional output and sensitivity tests are presented in Fig. S2.

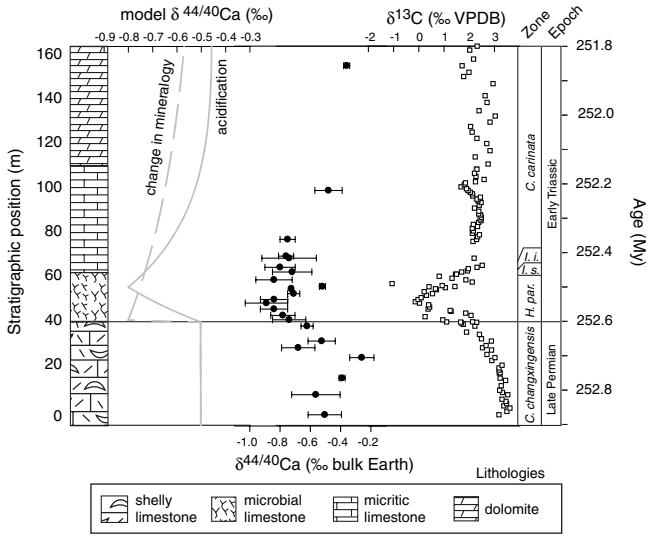

Fig. 2. Lithostratigraphy and calcium and carbon isotope data from the Dajiang section. Error bars indicate one standard deviation between replicate measurements. Carbon isotope data from ref. 65. Conodont zones from refs. 66 and 67. A constant depositional rate of 160 m/My is assumed for the numerical time scale in order to facilitate comparison to model output; the assumed rate is compatible with constraints on the platform (37) and an age of 252.6 My for the extinction horizon (68). Model output for the acidification scenario and the change in mineralogy are shown. See Table S4 for raw data.

$\delta^{44/40}Ca$ and no change in the marine calcium concentration (Fig. 1 and Fig. S2).

To constrain changes in global calcium cycling across the P/T transition, we analyzed the $\delta^{44/40}Ca$ of the micritic fraction of limestone samples from a P/T boundary section at Dajiang, in Guizhou Province, China. P/T boundary strata at Dajiang were deposited above the storm wave base on the Great Bank of Guizhou (GBG), an isolated carbonate platform within the Nanpanjiang Basin (32). The Nanpanjiang Basin is a deep-marine embayment in the Yangtze Block, which was located at approximately 12°N in the eastern Tethys during Early Triassic time (33). The section contains more than 50 m of diverse, fossiliferous packstone and grainstone of the Upper Permian Wujiaping Formation, which contains fusulinid and nonfusulinid foraminifers, calcareous green and red algae, rugose corals, crinoids, brachiopods, calcareous sponges, and gastropods (5, 34). The Wujiaping Formation is overlain by a 15-m-thick thrombolitic microbialite deposited in the immediate aftermath of the mass extinction (*Hindeodus parvus* conodont zone) (35), which contains a low-diversity assemblage of foraminifers, gastropods, and bivalves with rare echinoderms and calcitic and phosphatic brachiopods (4, 5). The microbialite is overlain by 1–2 m of molluscan and brachiopod packstone with rare echinoderms. Above the thin packstone interval are 47 m of thinly bedded, poorly bioturbated micritic limestone. The Lower Triassic section continues with 95 m of dolomite and dolomitized ooid-bearing cryptalgal laminate overlain by 225 m of peritidal limestone cycles (5, 36). Carbonate sediments continued to accumulate on the GBG through Middle Triassic time, reaching a total thickness of nearly 2 km before the platform drowned early in the Late Triassic (32). The GBG was buried in siliciclastic sediments during Late Triassic time, reaching a maximum burial depth of 2.5–3 km (37). Representative P/T boundary facies are illustrated in Fig. S1.

Results

Fig. 2 illustrates the P/T $\delta^{44/40}Ca$ and $\delta^{13}C$ records from the Dajiang section, along with age constraints from conodont biostratigraphy and geochronology and model output for the acidification scenario (our preferred scenario; see *Discussion* below) and a scenario involving a global shift from calcite- to aragonite-dominated carbonate deposition. The $\delta^{44/40}Ca$ averages approximately −0.6‰ in Permian strata. It decreases by ∼0.2‰ across the extinction horizon and by ∼0.3‰ from mean uppermost Permian values to the minimum in the basal Triassic (*H. parvus* zone), 8 m above the extinction horizon (Fig. 2). Although many individual pre- and postexcursion samples exhibit values within error of one another, the average value among samples within the excursion is significantly different from that for the preexcursion samples (Mann–Whitney test; $p = 0.0006$).

Several lines of evidence suggest that the $\delta^{44/40}Ca$ measurements are primary. The $\delta^{44/40}Ca$ shift coincides with the globally recognized negative $\delta^{13}C$ excursion (38), and the $\delta^{44/40}Ca$ values are significantly correlated with the $\delta^{13}C$ values (Pearson's $r = 0.62$; $p = 0.002$) but not with indicators of precipitation rate or diagenesis such as Sr/Ca, Mn/Sr, or $\delta^{18}O$ (Fig. S3). The preexcursion isotope composition (approximately −0.6‰ versus bulk Earth or +0.6‰ versus SRM-915a) is in agreement with Permian values from a Phanerozoic compilation of $\delta^{44/40}Ca$ values for carbonate rocks and well-preserved shell calcite (39). The light values in $\delta^{44/40}Ca$ continue from the microbialite facies into overlying micritic limestones before trending back toward preexcursion values (Fig. 2), suggesting that variation in $\delta^{44/40}Ca$ does not simply reflect differences among facies in either primary fractionation of calcium isotopes or later diagenetic alteration. Finally, similar to the $\delta^{13}C$ of carbonate rocks, there is far more calcium in the mineral than the pore fluids, helping buffer the $\delta^{44/40}Ca$ of carbonate minerals against alteration during burial diagenesis (40).

Discussion

The P/T boundary $\delta^{44/40}Ca$ excursion is inconsistent in direction with the prediction for ocean overturn and is larger in magnitude than the excursion predicted under the Strangelove Ocean or through a change in the isotope composition of weathered calcium. The $\delta^{44/40}Ca$ excursion is consistent in direction, magnitude, and

time scale with ocean acidification or a large shift in the proportional deposition of aragonite versus calcite. The $\delta^{44/40}$Ca excursion could also result from a local (not global) change in isotope fractionation during carbonate precipitation or a change in the local $\delta^{44/40}$Ca composition of seawater. Below, we consider the support for these local factors before addressing the global scenarios.

One possibility is that there is a temperature component to the $\delta^{44/40}$Ca excursion. Calcium isotope fractionation decreases with increasing temperature (41). Because temperatures increased across the P/T boundary (42), the temperature effect tends in the opposite direction from the observed excursion, reducing its apparent magnitude. The amount of warming across the boundary is poorly constrained, but an increase of 5–10 °C (43, 44) could reduce the fractionation by as much as 0.1–0.2‰ (26, 41). Thus, the negative excursion in seawater $\delta^{44/40}$Ca may be somewhat larger than reflected in the raw data.

An alternative mechanism for locally changing the $\delta^{44/40}$Ca of carbonate minerals is through a change in the local precipitation rate. Sr/Ca can serve as a proxy for precipitation rate (41); it is not correlated with $\delta^{44/40}$Ca in our samples (Fig. S3), suggesting that variation in precipitation rate does not explain the calcium isotope excursion. Moreover, the range of fractionation associated with typical modern carbonate precipitation rates is small (40 and references therein).

The isotope excursion could also reflect a change in the local, and not global, $\delta^{44/40}$Ca composition of seawater. There is no evidence for a significant $\delta^{44/40}$Ca gradient in the modern oceans (23), but stratigraphic variability in the isotope composition of ancient carbonates has been suggested to result from limited mixing between the open ocean and tectonic basins or epeiric seaways (45). The δ^{13}C excursion on the GBG, however, has been observed in carbonate sections across the globe (46, 47) and appears to be representative in terms of relative change in isotope composition as well as in absolute value. Any oceanographic gradient in $\delta^{44/40}$Ca would therefore need to have existed in the absence of a similar gradient in δ^{13}C. Consequently, we view a changing local $\delta^{44/40}$Ca gradient as unlikely.

A shift in mineralogy of carbonate sediment from calcite to aragonite could produce a negative excursion in $\delta^{44/40}$Ca of carbonate rocks because aragonite is ~0.6‰ lighter than calcite relative to source fluid (26). The observed $\delta^{44/40}$Ca excursion of 0.3‰ would thus require that half of the sediment pool in the ocean switched from calcite to aragonite across the extinction horizon. If the shift in mineralogy was only local, then the isotope recovery would require a local return to calcite-dominated sedimentation; if it was global and permanent, then the excursion decays because the global ocean approached a new steady state with a heavier $\delta^{44/40}$Ca of seawater because of the globally lighter $\delta^{44/40}$Ca in carbonate sediments (Fig. S2). The global scenario is consistent with the greater relative abundance of aragonite- versus calcite-producing skeletal animals globally in the Lower Triassic (48), with petrographic evidence for an originally aragonitic mineralogy for Early Triassic ooids and carbonate crystal fans (5), and with the similarity of Lower Triassic carbonate strata across the global tropics (8).

Finally, the excursion could reflect a decrease in the global $\delta^{44/40}$Ca of seawater. Such a decrease is most plausibly generated by ocean acidification (Fig. 1), which would reduce the carbonate ion concentration and carbonate saturation level of seawater and therefore allow calcium to accumulate. The calcium delivery flux is coupled to the dominant burial flux of carbonate sedimentation (F_{carb}) through the carbonate saturation state of seawater:

$$F_{carb} = k(\Omega - 1)^{\eta} \quad [1]$$

where k is a scaling constant, η is the order of the reaction [approximately 2 (refs. 10 and 49)], Ω is the saturation state with respect to calcite or aragonite ($\Omega = [Ca^{2+}][CO_3^{2-}]/K_{sp}$), and K_{sp} is the solubility product of the relevant carbonate mineral (50). Therefore, the effect of elevated calcium delivery via rivers, for example, is mitigated by an increase in Ω, which causes F_{carb} to increase concomitantly. An increase in seawater $[Ca^{2+}]$ is most likely to result from decreases in k and/or $[CO_3^{2-}]$. The loss of skeletal carbonate sinks following the end-Permian mass extinction (34) may have caused k to decrease because skeletal animals and algae had been expending metabolic energy to drive carbonate precipitation prior to the extinction. A decrease in $[CO_3^{2-}]$ and an increase in the calcium river flux are expected under scenarios of CO_2 or methane release previously proposed to account for the negative excursion in δ^{13}C (51–53): Because CO_2 is a weak acid (and methane oxidizes to CO_2 within years), rapid CO_2 input would lower ocean pH and $[CO_3^{2-}]$, reduce Ω and F_{carb}, and thereby allow calcium to accumulate in seawater while simultaneously warming the climate and accelerating the weathering of calcium-bearing rocks. If acidification caused the oceans to become undersaturated with respect to calcite, calcium could also have been released into seawater through dissolution of marine carbonate sediments.

The magnitude of excess calcium delivery required to explain our measured $\delta^{44/40}$Ca excursion under this acidification scenario can be calculated by mass balance, assuming a known isotopic composition of the calcium input and the starting size of the marine calcium reservoir. Because the mass extinction event occurred over less than 500 ky and likely less than 150 ky (54), we can approximate the event as instantaneous (see *SI Discussion*, Tables S1 and S2, and Fig. S4). Assuming that the input $\delta^{44/40}$Ca is isotopically similar to the river calcium flux and that the ocean $\delta^{44/40}$Ca was 1.4‰ heavier than our measured preextinction $\delta^{44/40}$Ca (i.e., fractionation similar to modern), we calculate an increase in seawater $[Ca^{2+}]$ of 21% (2.15 mM) for a 0.2‰ excursion or 36% (3.6 mM) for a 0.3‰ excursion (see *SI Discussion*). Here we have ignored the potential effects of changing temperature and mineralogy in order to investigate the effects of acidification alone. Because expected effects of temperature and mineralogy work in opposing directions (given increases in temperature and prevalence of aragonite) and the likely magnitudes of their effects are similar, in aggregate they may have mostly offset one another.

We favor the ocean acidification scenario over a change in sediment mineralogy as the explanation for the calcium isotope excursion because it also explains a wide range of geochemical, sedimentological, and paleontological observations associated with the P/T boundary not predicted by a shift in carbonate mineralogy alone. First, the synchronous deposition of microbialites and oolites across the global tropics within the *H. parvus* conodont zone (7, 8) could reflect rapid carbonate deposition resulting from enhanced silicate and carbonate weathering in the aftermath of a CO_2 release event. The weathering hypothesis can explain why synchronous, widespread deposition of these facies is confined to the earliest Triassic, despite the persistence of ocean anoxia (55) and skeleton-poor carbonate sediments (34) through much of Early Triassic time. Moreover, removing the calculated $2.2–3.6 \times 10^{18}$ mol of calcium from the oceans as calcium carbonate would translated to roughly 8–13 m of carbonate sediment on the 10^7 km^2 of Late Permian carbonate shelves (56), which is broadly consistent with the thickness of the microbialite and oolite deposits within the *H. parvus* zone (Table S3). Second, acidification can explain observations of submarine carbonate dissolution of beds immediately underlying the microbialite (8). Third, rapid CO_2 release can account for the negative excursion in δ^{13}C at the P/T boundary (46). Finally, ocean acidification can account for the preferential extinction of heavily calcified marine animals with limited ability to buffer calcifying fluids against changes in ambient water chemistry (17).

If the primary acid added to the oceans was CO_2, then the $\delta^{44/40}$Ca excursion can provide first-order constraints on the magnitude and C-isotope composition of carbon released because

each mole of CO_2 released would allow approximately 1 mol of calcium to be stored in the oceans (57). Assessing the source, magnitude, and isotope composition of carbon released at the P/T boundary has been challenging because the $\delta^{13}C$ excursion can potentially result from a smaller release from a ^{13}C-depleted source (e.g., biogenic methane) or a larger release from a less depleted reservoir (e.g., coal and basaltic magma). Berner (51) argued that only biogenic methane could account for the magnitude of the $\delta^{13}C$ excursion, but more recent studies of Siberian Traps intrusions suggest that the magnitude of carbon release may have been larger than previously suspected (22), opening the possibility of carbon release from less depleted reservoirs. One can estimate the $\delta^{13}C$ of the carbon source as a function of the initial total carbon given the estimated excess calcium delivery ($2.2–3.6 \times 10^{18}$ mol) and the excursion in $\delta^{13}C_{carb}$ (−3.6‰; cf. Fig. 2). The likely $\delta^{13}C$ composition of the CO_2 added on the basis of the above calculation is between −5 and −13‰ (Fig. 3). This calculation assumes that all acidifying power comes from CO_2. However, if emplacement of the Siberian Traps played a significant role (22), then sulfur release could account for as much as half of the acidification [volatile fluxes from flood basalts suggest a molar ratio of CO_2 to SO_2 release of 2.5:1 (58)]. Because H_2SO_4 can acidify the ocean without contributing to the decrease in $\delta^{13}C$, including its effects in the calculation requires a smaller, and thus isotopically lighter, carbon source. In this more conservative case, only $1.1–1.8 \times 10^{18}$ mol of CO_2 release would account for the $\delta^{13}C$ excursion and the $\delta^{13}C$ of the CO_2 would be between −11 and −28‰ (Fig. 3). Even under this more conservative scenario, the $\delta^{13}C$ of methane clathrates (−60‰) is far too negative to have been the primary source of carbon; the range of likely values instead points toward a mixture of carbon sources, which appear to have included a substantial component from carbonate rocks and/or mantle-derived volatiles.

Intrusion of Siberian Traps magmas through a thick sequence of carbonate sediments and coal (22) coeval with mass extinction (59) provides a mechanism for releasing sufficient quantities of CO_2 with the appropriate $\delta^{13}C$ composition through the production of thermogenic methane during the heating of coal (22) and CO_2-rich volatile phases during the incorporation of carbonate rocks into basaltic magma (60). Although previous studies have emphasized the release of carbon from methane clathrates or coal (51–53), $\delta^{44/40}Ca$ constraints instead suggest that carbon release associated with the end-Permian extinction may have included a substantial contribution from the incorporation of carbonate country rock into Siberian Traps magmas.

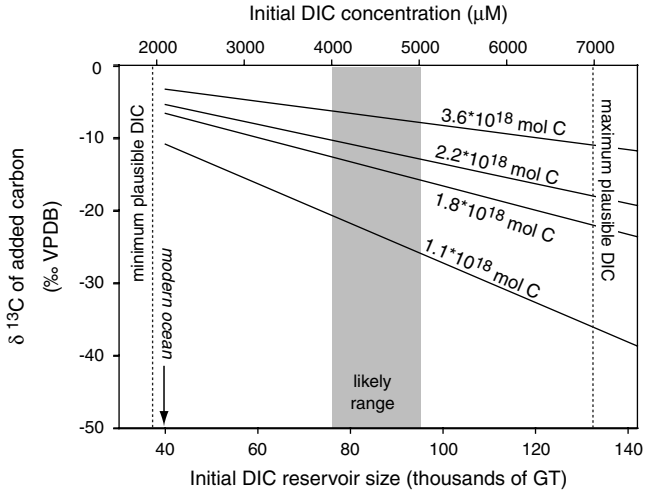

Fig. 3. Carbon isotope composition of carbon added in a P/T boundary perturbation as a function of the initial dissolved inorganic carbon content of the oceans, assuming a $\delta^{13}C$ excursion from +3.6 to 0‰. Results are shown for calculated upper (3.6×10^{18} mol; 43,200 GT) and lower (1.1×10^{18} mol; 13,200 GT) bounds on the amount of added carbon and intermediate values discussed in the text (1.8×10^{18} mol; 2.2×10^{18} mol).

The ocean acidification scenario that we favor for the P/T boundary is similar to that proposed for the Paleoecene-Eocene Thermal Maximum (PETM), where there is abundant evidence of a global decrease in the $\delta^{13}C$ and dissolution of deep-marine carbonate sediments (61) and possibly a negative excursion in $\delta^{44/40}Ca$ (62). Unlike the end-Permian event, however, the PETM is not associated with global mass extinction—only deep-sea benthic foraminifera were severely affected (63). Differences in the distribution of carbonate sediments between 250 and 55 million years ago may account for much of the contrast. At the PETM, as today, the oceans were buffered against acidification by extensive, fine-grained, unlithified carbonate sediments on the deep-sea floor, which could relatively rapidly dissolve to counter acidification (64). By contrast, the Late Permian deep sea contained no such carbonate buffer because Permian oceans lacked abundant pelagic carbonate producers such as coccolithophorids and planktonic foraminifers. Consequently, any buffering against acidification via dissolution of carbonate sediments could only have occurred more slowly in the less extensive, coarse-grained, mostly lithified, shallow-marine carbonate platform sediments or via chemical weathering of silicate and carbonate rocks on land. Thus, carbonate sediments may not only record critical information constraining the causes of end-Permian mass extinction; their spatial distribution in the oceans may also have been a key control on its severity.

Methods

Notation. Calculation of $\delta^{44/40}Ca$ follows standard delta notation:

$$\delta^{44/40}\mathrm{Ca} = \left[\frac{^{44}\mathrm{Ca}/^{40}\mathrm{Ca}_{\mathrm{sample}}}{^{44}\mathrm{Ca}/^{40}\mathrm{Ca}_{\mathrm{std}}} - 1\right] \times 1,000.$$

In this study, $\delta^{44/40}Ca$ values are referenced to a bulk Earth standard. To compare our numbers to those referenced to the SRM915a scale, our measured value of SRM915a (−1.2‰) can be added to the numbers reported in this work.

Sample Preparation. Samples collected from the outcrop were cut on a rock saw and subsequently ground and polished on a vibrating lapidary tray. The polished face was then drilled with a 1-mm dental bur to produce powder for analysis. Areas of micrite were selected for drilling in samples exhibiting macroscopic variation in carbonate phases. Early and late diagenetic cements, especially fracture-filling vein calcite, were avoided.

Calcium Isotope Analysis. Carbonates were dissolved in SEASTAR acetic acid. Calcium concentrations were determined, and 30-μg Ca aliquots were removed. A 42–48 calcium double spike was added to the aliquots and equilibrated in 5–8 mL of 2N nitric acid. The samples were loaded in 1N nitric acid onto ion separation columns filled with DOWEX® AG 50W-X8 resin. The samples were eluted in 2N nitric acid and dried down. These chemically separated, spiked samples were loaded onto Re filaments with phosphoric acid and measured on a multicollector thermal ionization mass spectrometer. Two replicates of each sample were run, and the standard deviation between replicate measurements is presented.

Trace Metal Analysis. For trace metal analysis, ~2 mg of dried, powdered limestone was dissolved in 1M acetic acid. After centrifugation, the supernatant was removed and subjected to trace metal analysis (Mn and Sr) as well as Ca and Mg analysis by using a Thermo Jarrell Ash IRIS Advantage/1000 Radial Inductively Coupled Argon Plasma Spectrometer with a solid state charge induction device detector.

Oxygen Isotope Analysis. For oxygen isotope analysis, samples were reacted with concentrated phosphoric acid at 90 °C in a common acid bath and then measured on a dual inlet mass spectrometer (VG Optima). Isotopic composition is reported in standard delta notation relative to the Vienna Pee Dee belemnite (VPDB) standard. Analytical precision was ±0.1‰ (2σ) on the basis of replicate measurements of a laboratory standard.

Geochemical Model. Coupled models of the global calcium and carbon cycles were constructed assuming a one-box ocean and steady-state conditions prior to perturbation.

ACKNOWLEDGMENTS. We thank S. Brown, T. Owens, and A. Jost for assistance with analyses. This study was supported by the Miller Institute for Basic Research and the Canadian Institute for Advanced Research (fellowships to A.V. T.), the Petroleum Research Fund of the American Chemical Society [Grant 45329-G8 (to J.L.P.); Grant 40948 (to D.J.L.), the National Geographic Society [Grant 8102-06 (to J.L.P.)], the National Science Foundation [CAREER Award (to A.P.); Grant EAR-0807377 (to J.L.P.)], and National Aeronautics and Space Administration [Grant NNX09AN67G (to J.L.P.)].

1. Kershaw S, Guo L, Swift A, Fan JS (2002) Microbialites in the Permian-Triassic boundary interval in Central China: Structure, age and distribution. *Facies* 47:83–89.
2. Kershaw S, et al. (2007) Earliest Triassic microbialites in the South China block and other areas: Controls on their growth and distribution. *Facies* 53:409–425.
3. Kershaw S, Zhang TS, Lan GZ (1999) A microbialite carbonate crust at the Permian-Triassic boundary in South China, and its palaeoenvironmental significance. *Palaeogeogr Palaeoclimatol Palaeoecol* 146:1–18.
4. Lehrmann DJ (1999) Early Triassic calcimicrobial mounds and biostromes of the Nanpanjiang basin, south China. *Geology* 27:359–362.
5. Lehrmann DJ, et al. (2003) Permian-Triassic boundary sections from shallow-marine carbonate platforms of the Nanpanjiang Basin, south China: Implications for oceanic conditions associated with the end-Permian extinction and its aftermath. *Palaios* 18:138–152.
6. Baud A, Cirilli S, Marcoux J (1997) Biotic response to mass extinction: The lowermost Triassic microbialites. *Facies* 36:238–242.
7. Baud A, Richoz S, Marcoux J (2005) Calcimicrobial cap rocks from the basal Triassic units: Western Taurus occurrences (SW Turkey). *C R Palevol* 4:569–582.
8. Payne JL, et al. (2007) Erosional truncation of uppermost Permian shallow-marine carbonates and implications for Permian-Triassic boundary events. *Geol Soc Am Bull* 119:771–784.
9. Sano H, Nakashima K (1997) Lowermost Triassic (Griesbachian) microbial bindstone-cementstone facies, southwest Japan. *Facies* 36:1–24.
10. Rampino MR, Caldeira K (2005) Major perturbation of ocean chemistry and a 'Strangelove Ocean' after the end-Permian mass extinction. *Terra Nova* 17:554–559.
11. Isozaki Y (1997) Permo-triassic boundary superanoxia and stratified superocean: Records from lost deep sea. *Science* 276:235–238.
12. Grice K, et al. (2005) Photic zone euxinia during the Permian-Triassic superanoxic event. *Science* 307:706–709.
13. Nielsen JK, Shen Y (2004) Evidence for sulfidic deep water during the Late Permian in the East Greenland Basin. *Geology* 32:1037–1040.
14. Kump LR, Pavlov A, Arthur MA (2005) Massive release of hydrogen sulfide to the surface ocean and atmosphere during intervals of oceanic anoxia. *Geology* 33:397–400.
15. Knoll AH, Bambach RK, Canfield DE, Grotzinger JP (1996) Comparative Earth history and Late Permian mass extinction. *Science* 273:452–457.
16. Grotzinger JP, Knoll AH (1995) Anomalous carbonate precipitates: Is the Precambrian the key to the Permian?. *Palaios* 10:578–596.
17. Knoll AH, Bambach RK, Payne JL, Pruss S, Fischer WW (2007) Paleophysiology and end-Permian mass extinction. *Earth Planet Sc Lett* 256:295–313.
18. Retallack GJ, Jahren AH (2008) Methane release from igneous intrusion of coal during Late Permian extinction events. *J Geol* 116:1–20.
19. Heydari E, Arzani N, Hassanzadeh J (2008) Mantle plume: The invisible serial killer—Application to the Permian-Triassic boundary mass extinction. *Palaeogeogr Palaeoclimatol Palaeoecol* 264:147–162.
20. Heydari E, Hassanzadeh J (2003) Deev Jahi Model of the Permian-Triassic boundary mass extinction: A case for gas hydrates as the main cause of biological crisis on Earth. *Sediment Geol* 163:147–163.
21. Svensen H, et al. (2004) Release of methane from a volcanic basin as a mechanism for initial Eocene global warming. *Nature* 429:542–545.
22. Svensen H, et al. (2009) Siberian gas venting and the end-Permian environmental crisis. *Earth Planet Sc Lett* 277:490–500.
23. Zhu P, Macdougall JD (1998) Calcium isotopes in the marine environment and the oceanic calcium cycle. *Geochim Cosmochim Acta* 62:1691–1698.
24. Fantle MS, DePaolo DJ (2005) Variations in the marine Ca cycle over the past 20 million years. *Earth Planet Sc Lett* 237:102–117.
25. Lemarchand D, Wasserburg GJ, Papanastassiou DA (2004) Rate-controlled calcium isotope fractionation in synthetic calcite. *Geochim Cosmochim Acta* 68:4665–4678.
26. Gussone N, et al. (2005) Calcium isotope fractionation in calcite and aragonite. *Geochim Cosmochim Acta* 69:4485–4494.
27. DePaolo DJ (2004) Calcium isotopic variations produced by biological, kinetic, radiogenic and nucleosynthetic processes. *Rev Mineral Geochem* 55:255–288.
28. De La Rocha CL, DePaolo DJ (2000) Isotopic evidence for variations in the marine calcium cycle over the Cenozoic. *Science* 289:1176–1178.
29. Hotinski RM, Bice KL, Kump LR, Najjar RG, Arthur MA (2001) Ocean stagnation and end-Permian anoxia. *Geology* 29:7–10.
30. Zhang R, Follows MJ, Grotzinger JP, Marshall J (2001) Could the Late Permian deep ocean have been anoxic?. *Paleoceanography* 16:317–329.
31. Meyer KM, Kump LR, Ridgwell A (2008) Biogeochemical controls on photic-zone euxinia during the end-Permian mass extinction. *Geology* 36:747–750.
32. Lehrmann DJ, Wei JY, Enos P (1998) Controls on facies architecture of a large Triassic carbonate platform: The Great Bank of Guizhou, Nanpanjiang Basin, South China. *J Sediment Res* 68:311–326.
33. Enos P, et al. (2006) *Triassic Evolution of the Yangtze Platform in Guizhou Province, People's Republic of China: Geological Society of America Special Paper 417* (Geological Society of America, Boulder, CO).
34. Payne JL, Lehrmann DJ, Wei J, Knoll AH (2006) The pattern and timing of biotic recovery from the end-Permian extinction on the Great Bank of Guizhou, Guizhou Province, China. *Palaios* 21:63–85.
35. Chen J, Beatty TW, Henderson CM, Rowe H (2009) Conodont biostratigraphy across the Permian-Triassic boundary at the Dawen section, Great Bank of Guizhou, Guizhou Province, South China: Implications for the Late Permian extinction and correlation with Meishan. *J Asian Earth Sci* 36:442–458.
36. Lehrmann DJ, Wan Y, Wei JY, Yu YY, Xiao JF (2001) Lower Triassic peritidal cyclic limestone: An example of anachronistic carbonate facies from the Great Bank of Guizhou, Nanpanjiang Basin, Guizhou Province, South China. *Palaeogeogr Palaeoclimatol Palaeoecol* 173:103–123.
37. Lehrmann DJ, et al. (2007) Impact of differential tectonic subsidence on isolated carbonate-platform evolution: Triassic of the Nanpanjiang Basin, south China. *AAPG Bull* 91:287–320.
38. Corsetti FA, Baud A, Marenco PJRS (2005) Summary of Early Triassic carbon isotope records. *C R Palevol* 4:405–418.
39. Farkas J, et al. (2007) Calcium isotope record of Phanerozoic oceans: Implications for chemical evolution of seawater and its causative mechanisms. *Geochim Cosmochim Acta* 71:5117–5134.
40. Fantle MS, DePaolo DJ (2007) Ca isotopes in carbonate sediment and pore fluid from ODP site 807A: The Ca^{2+}(aq)-calcite equilibrium fractionation factor and calcite recrystallization rates in Pleistocene sediments. *Geochim Cosmochim Acta* 71:2524–2546.
41. Tang J, Dietzel M, Böhm F, Köhler SJ, Eisenhauer A (2008) Sr^{2+}/Ca^{2+} and $^{44}Ca/^{40}Ca$ fractionation during inorganic calcite formation: II. Ca isotopes. *Geochim Cosmochim Acta* 72:3733–3745.
42. Korte C, et al. (2004) Carbon, sulfur, oxygen and strontium isotope records, organic geochemistry and biostratigraphy across the Permian/Triassic boundary in Abadeh, Iran. *Int J Earth Sci* 93:565–581.
43. Holser WT, et al. (1989) A unique geochemical record at the Permian Triassic boundary. *Nature* 337:39–44.
44. Retallack GJ (1999) Postapocalyptic greenhouse paleoclimate revealed by earliest Triassic paleosols in the Sydney Basin, Australia. *Geol Soc Am Bull* 111:52–70.
45. Holmden C (2009) Ca isotope study of Ordovician dolomite, limestone, and anhydrite in the Williston Basin: Implications for subsurface dolomitization and local Ca cycling. *Chem Geol* 268:180–188.
46. Baud A, Magaritz M, Holser WT (1989) Permian-Triassic of the Tethys—Carbon isotope studies. *Geol Rundsch* 78:649–677.
47. Musashi M, Isozaki Y, Koike T, Kreulen R (2001) Stable carbon isotope signature in mid-Panthalassa shallow-water carbonates across the Permo-Triassic boundary: Evidence for C-13-depleted superocean. *Earth Planet Sc Lett* 191:9–20.
48. Kiessling W, Aberhan M, Villier L (2008) Phanerozoic trends in skeletal mineralogy driven by mass extinctions. *Nat Geosci* 1:527–530.
49. Burton EA, Walter LM (1987) Relative precipitation rates of aragonite and Mg calcite from seawater—Temperature or carbonate ion control?. *Geology* 15:111–114.
50. Opdyke BN, Wilkinson BH (1993) Carbonate mineral saturation state and cratonic limestone accumulation. *Am J Sci* 293:217–234.
51. Berner RA (2002) Examination of hypotheses for the Permo-Triassic boundary extinction by carbon cycle modeling. *Proc Natl Acad Sci USA* 99:4172–4177.
52. Krull ES, Retallack GJ (2000) delta C-13 depth profiles from paleosols across the Permian-Triassic boundary: Evidence for methane release. *Geol Soc Am Bull* 112:1459–1472.
53. Erwin DH (1993) *The Great Paleozoic Crisis: Life and Death in the Permian* (Columbia Univ Press, New York).
54. Bowring SA, et al. (1998) U/Pb zircon geochronology and tempo of the end-Permian mass extinction. *Science* 280:1039–1045.
55. Wignall PB, Twitchett RJ (2002) *Catastrophic Events and Mass Extinctions; Impacts and Beyond: Geological Society of America Special Publication 356*, eds C Koeberl and KG MacLeod (Geological Society of America, Boulder, CO), pp 395–413.
56. Walker LJ, Wilkinson BH, Ivany LC (2002) Continental drift and Phanerozoic carbonate accumulation in shallow-shelf and deep-marine settings. *J Geol* 110:75–87.
57. Caldeira K, Wickett ME (2005) Ocean model predictions of chemistry changes from carbon dioxide emissions to the atmosphere and ocean. *J Geophys Res* 110:C09S04.
58. Self S, Thordarson T, Widdowson M (2005) Gas fluxes from flood basalt eruptions. *Elements* 1:283–287.
59. Reichow MK, et al. (2009) The timing and extent of the eruption of the Siberian Traps large igneous province: Implications for the end-Permian environmental crisis. *Earth Planet Sc Lett* 277:9–20.
60. Iacono Marziano G, Gaillard F, Pichavant M (2008) Limestone assimilation by basaltic magmas: An experimental re-assessment and application to Italian volcanoes. *Contrib Mineral Petr* 155:719–738.
61. Zachos JC, et al. (2005) Rapid acidification of the ocean during the Paleocene-Eocene thermal maximum. *Science* 308:1611–1615.
62. Griffith EM, Paytan A (2008) *Proceedings of the American Geophysical Union Annual Meeting* (Am Geophysical Union, San Francisco) p B14B-05.
63. Thomas E, Shackleton NJ (1996) The Paleocene-Eocene benthic foraminiferal extinction and stable isotope anomalies. *Geol Soc SP* 101:401–441.

64. Archer D, Kheshgi H, Maier-Reimer E (1997) Multiple timescales for neutralization of fossil fuel CO_2. *Geophys Res Lett* 24:405–408.
65. Payne JL, et al. (2004) Large perturbations of the carbon cycle during recovery from the end-Permian extinction. *Science* 305:506–509.
66. Ezaki Y, Liu J, Nagano T, Adachi N (2008) Geobiological aspects of the earliest Triassic microbialites along the southern periphery of the Tropical Yangtze Platform: Initiation and cessation of a microbial regime. *Palaios* 23:356–369.
67. Krull ES, et al. (2004) Stable carbon isotope stratigraphy across the Permian-Triassic boundary in shallow marine carbonate platforms, Nanpanjiang Basin, south China. *Palaeogeogr Palaeoclimatol Palaeoecol* 204:297–315.
68. Mundil R, Ludwig KR, Metcalfe I, Renne PR (2004) Age and timing of the Permian mass extinctions: U/Pb dating of closed-system zircons. *Science* 305:1760–1763.